



# Discussion on fabrication accuracy of infrared topological photonic structures using hyperspectral Fourier image spectroscopy

SHO OKADA,<sup>1,4</sup> TOMOHIRO AMEMIYA,<sup>1,2,5</sup> HIBIKI KAGAMI,<sup>1</sup> YAHUI WANG,<sup>1</sup>  
NOBUHIKO NISHIYAMA,<sup>1,2</sup> AND XIAO HU<sup>3</sup>

<sup>1</sup>Department of Electrical and Electronic Engineering, Tokyo Institute of Technology, Tokyo 152-8552, Japan

<sup>2</sup>Institute of Innovative Research (IIR), Tokyo Institute of Technology, Tokyo 152-8552, Japan

<sup>3</sup>International Center for Materials Nanoarchitectonics (WPI-MANA), National Institute for Materials Science, Tsukuba 305-0044, Japan

<sup>4</sup>e-mail: okada.s.ah@m.titech.ac.jp

<sup>5</sup>e-mail: amemiya.t.ab@m.titech.ac.jp

Received 2 February 2022; revised 8 August 2022; accepted 8 August 2022; posted 9 August 2022; published 22 August 2022

Compared to conventional periodic nanostructures such as photonic crystals, topological photonic systems require more precise fabrication techniques due to the need to place multiple dielectrics at appropriate positions within a unit cell, and this becomes particularly remarkable in the optical communication band. In this paper, observing photonic band structures by using hyperspectral Fourier image spectroscopy, we quantitatively discuss the fabrication accuracy of typical topological photonic systems in which triangle nanoholes were arranged in a deformed honeycomb lattice with  $C_{6v}$  symmetry. Here the size and corner radius of triangle nanoholes were precisely controlled using shape correction electron beam lithography. The results showed that the fabrication error must be controlled to below  $\sim 10$  nm for the size and  $\sim 30$  nm for the corner radius, in order to achieve the desired topological edge state that occurs at the interface between two photonic structures different in topology. © 2022 Optica Publishing Group

<https://doi.org/10.1364/JOSAB.454949>

## 1. INTRODUCTION

Topological photonics brings the concept of topology from mathematics into the field of photonics, which allows us to systematically handle information resulting from the topology of light, such as circular polarization (spin of light) and optical vortices (orbital angular momentum of light) [1–10]. Especially, topological photonic crystals based on crystalline symmetry where dielectrics arranged in a deformed honeycomb lattice with  $C_{6v}$  symmetry are suitable for the conventional semiconductor nanoprocessing technology [5]. Using the above structure, various studies are being conducted on their application in different frequency bands [11–19].

One of the most well-known phenomena in topological photonic systems is the topological edge state that occurs at the interface between two photonic structures different in topology. It is possible to realize unprecedented optical phenomena such as optical spin-dependent unidirectional propagation and sharp bend-tolerant low-loss optical propagation [6,20–24]. Furthermore, laser oscillations caused by topological phenomena have been demonstrated [25,26]. The systems that use light confinement by a topological interface due to difference in mode parity [27], spin-momentum locking at a topological interface [28], valley photonics [29–31], and a topological

corner state [32,33] have been explored, which are extremely promising as coherent light sources for circularly polarized light and optical vortices.

In the above-mentioned topological photonic systems, structures inside a unit cell are tuned to induce the nontrivial photonic topology. Thus, careful structural designs and high-precision fabrications are required as compared to conventional photonic crystals. This is particularly noticeable in the optical communication band, which is considered to be the most useful application area for these systems. Although numerous research institutes have developed such systems, there is no study that quantitatively discusses the accuracy required in the actual fabrication of topological photonic systems (only a few papers touched the structural accuracy required for topological photonic crystals [21,24,31], but that fact has not been evaluated experimentally). In this study, hyperspectral Fourier image spectroscopy was used to evaluate the optical characteristics of typical topological photonic structures in which dielectrics with  $C_{6v}$  symmetry are arranged in a honeycomb lattice, and the fabrication accuracy was quantitatively discussed.

The rest of this paper is organized as follows: In Section 2, we discuss the structural dependence of the optical characteristics of the typical topological photonic crystal used in this study

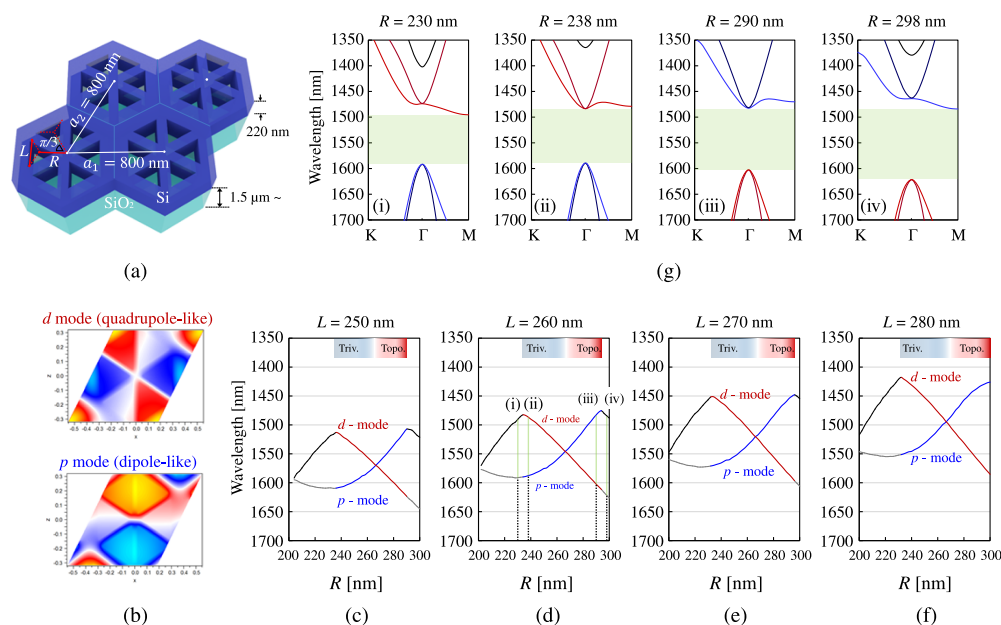


**Fig. 1.** (a) Schematic image of topological photonic structure in which nanoholes with  $C_{6v}$  symmetry are arranged in a honeycomb lattice on an SOI substrate. (b) Magnetic field distribution in one unit cell. (c)–(f) Calculated wavelengths (i.e., energies) above and below the bandgap edge in the band structure of each structure with different  $L$ . The inset diagram shows the range of structures that can create edge states. (g) Calculated photonic band structures of topological photonic structures with different  $R$  [regions (i)–(iv) in Fig. 1(d)].

through theoretical calculations. In Section 3, we describe the fabrication of a structure with a design that is close to the theoretical design. The fabrication process introduces proximity effect correction. In Section 4, we perform the optical evaluation of the structure using hyperspectral Fourier image spectroscopy and quantitatively discuss the accuracy required in the fabrication of a topological photonic system. Section 5 provides the conclusions.

## 2. THEORETICAL OPTICAL CHARACTERISTICS OF TOPOLOGICAL PHOTONIC STRUCTURES WITH $C_{6v}$ SYMMETRY

As a photonic structure with  $\mathbb{Z}_2$  topology, we used the structure in which nanoholes with  $C_{6v}$  symmetry are arranged in a honeycomb lattice on a silicon-on-insulator (SOI) substrate with a Si core thickness of 220 nm [Fig. 1(a)]. The period,  $a_0$ , of the deformed honeycomb lattice was fixed at 800 nm. The structural parameters were the distance,  $R$ , from the center of the hexagonal unit cell to the center of the nanohole and the length,  $L$ , of one side of the nanohole.

Figures 1(c)–1(f) show the wavelengths (i.e., energies) above and below the bandgap edge in the band structure of each structure calculated using the plane wave expansion method (the number of plane waves used to reach convergence is 128). For  $R = 260 - 270$  nm, the inversion of the  $p$ -wave mode and  $d$ -wave mode is observed at the  $\Gamma$  point of the band structure, which induces the desired photonic topology (hereinafter referred to as topological/trivial after/before band inversion).

In Figs. 1(c)–1(f), the energy reaches a maximum at a certain value of  $R$  at the upper bandgap edge. This is because the points that constitute the bandgap shift from the  $\Gamma$  point (direct gap)

to the M point (indirect gap), as shown in Fig. 1(g). As a direct bandgap is required at  $\Gamma$  points to realize an accurate topological edge state, only the areas such as those shown at the top of Figs. 1(b)–1(f) are considered.

When  $L$  increases by 10 nm, the band shifts to the shorter wavelength side by 20 nm while maintaining its shape. In addition, the range of  $R$  in which there is a direct bandgap at  $\Gamma$  points increases.

These results show that, to generate a topological edge state using a typical structure for a target wavelength of 1550 nm (optical communication band), the fabrication error must be controlled to below  $\sim 20$  nm for  $R$  and  $\sim 10$  nm for  $L$ . Here, the value of  $R$  can be sufficiently realized using an electron beam (EB) lithography or stepper lithography. However, for  $L$ , considering that the corners of triangular nanoholes are generally rounded, extremely high fabrication precision is required. In the next section, we will discuss the details.

## 3. FABRICATION OF TOPOLOGICAL PHOTONIC STRUCTURE USING SHAPE CORRECTION ELECTRON BEAM LITHOGRAPHY

We used EB lithography to fabricate the structure. A fabricated structure is usually different from its computer-aided design (CAD) owing to the spread of the EB inside the resist and the nonuniformity of the gas distribution derived from the surface shape during etching [34]. This effect is particularly strong in the acute-angled structures used in topological photonics, and rounded corners are unavoidable in fabricated structures. The above generally has a large effect on the appearance of topological edge states. (Conventional photonic crystals do not have the above problem. See Appendix A for more information.)

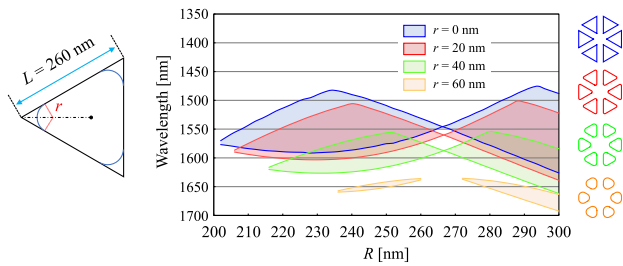


**Fig. 2.** Calculated bandgap edge when the shape of a dielectric hexagonal unit cell changes from an ideal equilateral triangle owing to the rounding of its corners. One side of the triangular nanohole ( $L$ ) was fixed at 260 nm.  $r$ , radius of curvature.

Figure 2 shows the changes in the bandgap edge when the shape of a dielectric hexagonal unit cell is tuned from an ideal equilateral triangle owing to the rounding of its corners. In this analysis,  $R$  was changed, and  $L$  was fixed at 260 nm. The region shown in blue in Fig. 2 is same as that in Fig. 1(d). As the radius of curvature,  $r$ , of the triangular nanohole increases, the entire band shifts to the long wavelength side, and the width of the bandgap gradually decreases because degeneracy is resolved at the  $\Gamma$  point on the trivial side. As the narrowing of the band leads to the leakage of light during topological edge transmission, a radius of curvature of approximately 30 nm or less is suitable for obtaining a desired topological edge state. This is required for performing proximity effect correction or shape correction during EB lithography.

We applied ZEP520A (first slope, 10 s; second slope, 2000 rpm  $\times$  120 s; third slope, 10 s; thickness, 500 nm) on an SOI substrate with a Si core thickness of 220 nm. Thereafter, we formed the pattern through EB lithography (JEOL JBX-6300UA; acceleration voltage, 50 kV; beam current, 100 pA; dose, 170  $\mu\text{C}/\text{cm}^2$ ). Then, we prepared the structure by etching the Si layer through inductively coupled plasma reactive ion etching using  $\text{CF}_4 - \text{SF}_6$  mixed gas (mixing ratio, 9:2) (Samco RIE-101iPH; ICP power, 160 W; bias power, 60 W; pressure, 0.05 Pa; etching time, 7 min).

ZEP520A, which was used as the mask, was removed via  $\text{O}_2$  ashing (Samco RIE-101iPH; ICP power, 100 W; bias power, 0 W; pressure, 0.05 Pa; etching time, 40 min), treatment with a piranha solution ( $\text{H}_2\text{SO}_4 : \text{H}_2\text{O}_2 = 3 : 1$ ), and treatment with a high-performance liquid (Novec 7200). To realize a triangular nanohole with the above-mentioned radius of curvature or lower, shape correction [optical proximity correction

(OPC)] lithography was introduced based on empirical big data processing. Figure 3(a) shows a shape-corrected triangular nanohole pattern. Specifically, the shape is such that the vicinity of the apex of the triangle is narrowed, and a circular pattern is placed at the center of the apex. Figure 3(b) shows the scanning electron microscope images of the triangular nanoholes with and without shape correction. As a result, the corner radius of the triangular nanoholes without shape correction was 50 nm, which was insufficient to generate a topological edge state. On the other hand, by introducing shape correction, the corner radius could be suppressed to about 30 nm. In the next section, we will discuss the above effects quantitatively by observing the topological bandgap by using hyperspectral Fourier image spectroscopy.

#### 4. BAND STRUCTURE EVALUATION OF TOPOLOGICAL PHOTONIC STRUCTURES

To discuss fabrication accuracy of topological photonic structures, we observed the photonic band structure by using hyperspectral Fourier image spectroscopy covering the wavelengths ranging from 850 to 1800 nm. First, light from a wideband white light source (Bentham Ltd. WLS100; wavelength range, 300–2500 nm) was passed through a 60 $\times$  objective lens (NA 0.9, Olympus Plan Fluorite Objective, UPLFLN60X), and it was incident perpendicular to the structure. Next, the Fourier image of the light scattered from the structure was observed using an infrared camera through the 4f optical system. A tunable filter (CRI, VariSpec LNIR; bandwidth, 6 nm) was placed in front of the infrared camera to obtain diffraction patterns at arbitrary wavelengths in a range of 850–1800 nm. The photonic band structure was obtained using this configuration via the following procedure (considering its high speed and versatility, a series of operations was fully automated using software): First, the Fourier image of the light scattered from the structure was observed while changing the center wavelength of the tunable filter. Next, for the obtained Fourier image, the intensity information along a specified path was measured and converted into the intensity distribution of the specific energy in the reciprocal lattice space. The photonic band diagram was reconstructed by performing the same operation for all wavelengths and arranging them in a two-dimensional space. (For details of this measurement method, including measurement time and resolution, also see [35]).

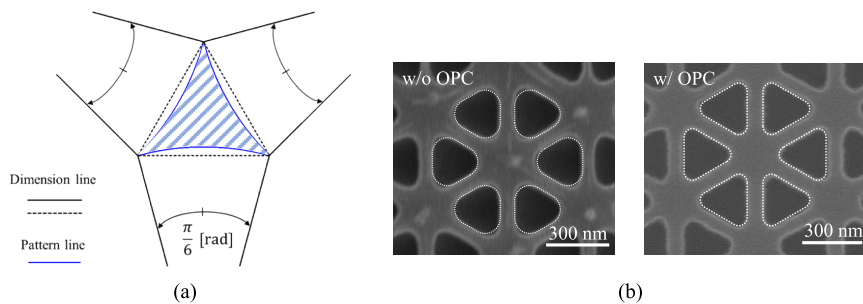


**Fig. 3.** (a) Shape correction EB lithography pattern for triangular nanohole. The areas exposed by EB lithography are indicated by blue shaded lines. (b) Scanning electron microscope images of the triangular nanoholes with and without shape correction. Corner radii of the triangular nanoholes with and without shape correction are 50 nm and less than 30 nm, respectively.

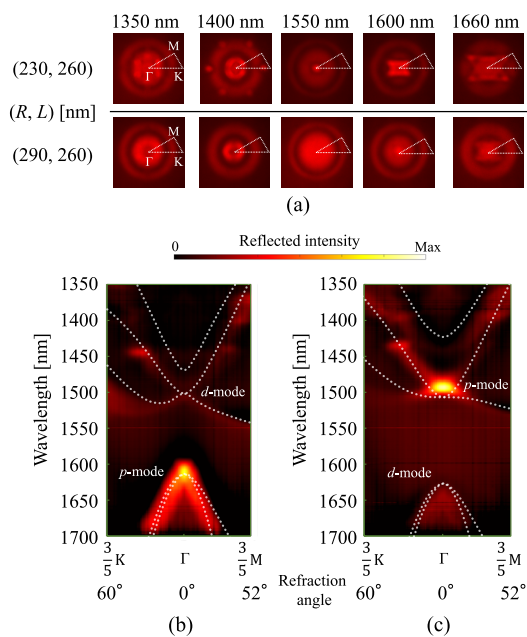


**Fig. 4.** (a) Fourier image of the scattered light from topological photonic structures at each wavelength. (b) and (c) Reconstructed band structures of photonic crystals with different topologies, which was derived from the intensity along the  $\Gamma$ -K-M path in measured Fourier images (range of the Brillouin zone in each direction was determined by the effective angle of the objective lens using hyperspectral Fourier image spectroscopy). The dotted line is the analysis result when the radius of curvature  $r$  is 30 nm.

Figure 4 shows the measurement results for two typical structures with different topologies  $[(R, L) = (230 \text{ nm}, 260 \text{ nm}), (290 \text{ nm}, 260 \text{ nm})]$ . Figure 4(a) shows the Fourier image of the light scattered from the structure, where clear changes due to the photonic band are observed at each wavelength. Figures 4(b) and 4(c) show the band structures reconstructed by measuring the intensities along the  $\Gamma$ -K-M path corresponding to the deformed honeycomb lattice in Fig. 4(a). In band structure, the bandgap is close to  $1.5 \mu\text{m}$ , which is the optical communication wavelength band. Noticeably, the intensities of the upper and lower bandgap edges close to the  $\Gamma$  point are reversed. In general, the reflection intensity of the  $d$ -wave in the electromagnetic mode tends to be weaker than that of the  $p$ -wave [36]. Therefore, the experimental results show that the electromagnetic modes of the  $p$ -wave and  $d$ -wave are band inverted, which agrees with the theoretical estimation.

Figure 5(a) shows the band structures for more values of  $R$  and  $L$ . When the bandgap shrinks and, thus, the  $p$  mode and  $d$  mode get close to each other in frequency similar to graphene (gapless), the reflectance from the structure becomes extremely weak. This can be used to determine the switching of the bands in experiments. Figure 5(b) shows the energy (wavelength) above and below the bandgap edge, read from the band structures shown in Fig. 5(a). Figure 5(b) also shows analysis results for photonic structures with ideal triangle nanoholes and with triangle nanoholes having a corner radius of 20 and 30 nm. Compared to the analysis results for the ideal triangular shape, the bandgap edge entirely shifts to the long wavelength side, and

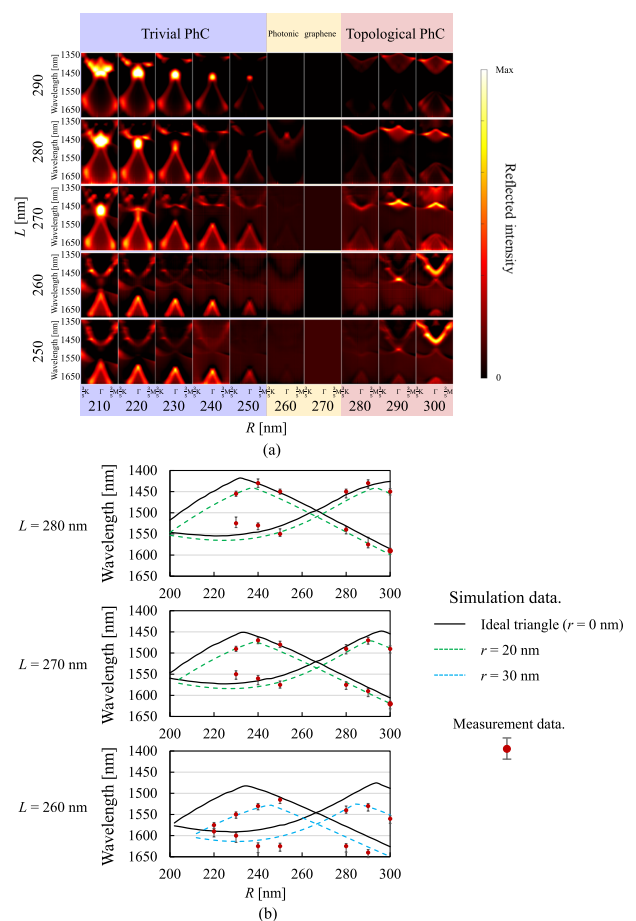


**Fig. 5.** (a) Measured band structures of photonic crystals with different dimensions. (b) Measured wavelengths (i.e., energies) of the upper and lower band edges in the band structures shown in (a) and corresponding simulation results plotted with solid and dashed lines, respectively.

the width of the bandgap decreases, which is consistent with the trend shown in Fig. 2.

As a result, from band structures obtained by hyperspectral Fourier image spectroscopy, a corner radius of the triangular nanoholes was less than 30 nm, which was sufficient to generate a topological edge state.

## 5. CONCLUSION

In this study, hyperspectral Fourier image spectroscopy was used to evaluate the optical characteristics of topological photonic structures consisting of triangle nanoholes arranged into deformed honeycomb lattices with  $C_{6v}$  symmetry, and the fabrication accuracy was quantitatively discussed. Here the structural parameters  $L$  and  $r$  referring to the size and corner radius of triangle nanoholes were precisely controlled using shape correction EB lithography. The results showed that the fabrication error must be controlled to below  $\sim 10 \text{ nm}$  for  $L$  and  $\sim 30 \text{ nm}$  for  $r$ , in order to achieve the desired topological edge state that occurs at the interface between two photonic structures different in topology. This means that considerably high accurate fabrication technology is required for application of topological photonics in future optical communication systems.

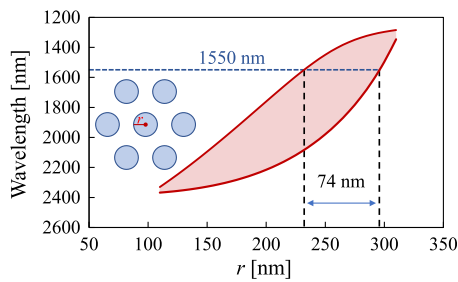


**Fig. 6.** Gap map of conventional photonic crystals with circular holes arranged in a triangular lattice.

## APPENDIX A

Figure 6 shows the results of the gap map analysis of conventional photonic crystals with circular holes arranged in a triangular lattice. The plane wave expansion method was used for the analysis, and the period of the triangular lattice was 640 nm. When designing the photonic bandgap to enter at 1550 nm, the fabrication error tolerance for the radius  $r$  was estimated to be 74 nm. In the above photonic crystal, it is hard for the proximity effect of EB lithography to occur because there are no sharp edges in the components. Moreover, considering that the etching gas entry is isotropic, the fabrication error is at most 10 nm. These facts allow us to say that the tolerance of 74 nm is sufficient. On the other hand, topological photonic crystals used in this study have multiple elements with sharp angles within the unit cell, which can lead to large fabrication errors from the designed shape. To avoid this, it is necessary to introduce shape correction EB lithography, which is mentioned in this paper.

**Funding.** Ministry of Internal Affairs and Communications (182103111); Japan Society for the Promotion of Science (19H02193, 21J14822); Core Research for Evolutional Science and Technology (JPMJCR18T4).

**Disclosures.** The authors declare no conflicts of interest.

**Data availability.** Data underlying the results presented in this paper are not publicly available at this time but may be obtained from the authors upon reasonable request.

## REFERENCES

- F. D. M. Haldane and S. Raghu, "Possible realization of directional optical waveguides in photonic crystals with broken time-reversal symmetry," *Phys. Rev. Lett.* **100**, 013904 (2008).
- Z. Wang, Y. Chong, J. D. Joannopoulos, and M. Soljacic, "Observation of unidirectional backscattering-immune topological electromagnetic states," *Nature* **461**, 772–775 (2009).
- M. Hafezi, S. Mittal, J. Fan, A. Migdall, and J. M. Taylor, "Imaging topological edge states in silicon photonics," *Nat. Photonics* **7**, 1001–1005 (2013).
- L. Lu, J. D. Joannopoulos, and M. Soljacic, "Topological photonics," *Nat. Photonics* **8**, 821–829 (2014).
- L.-H. Wu and X. Hu, "Scheme for achieving a topological photonic crystal by using dielectric material," *Phys. Rev. Lett.* **114**, 223901 (2015).
- A. B. Khanikaev and G. Shvets, "Two-dimensional topological photonics," *Nat. Photonics* **11**, 763–773 (2017).
- Y. Wu, C. Li, X. Hu, Y. Ao, Y. Zhao, and Q. Gong, "Applications of topological photonics in integrated photonic devices," *Adv. Opt. Mater.* **5**, 1700357 (2017).
- B.-Y. Xie, H.-F. Wang, X.-Y. Zhu, M.-H. Lu, Z. D. Wang, and Y.-F. Chen, "Photonics meets topology," *Opt. Express* **26**, 24531–24550 (2018).
- Y. Li, Y. Sun, W. Zhu, Z. Guo, J. Jiang, T. Kariyado, H. Chen, and X. Hu, "Topological LC-circuits based on microstrips and observation of electromagnetic modes with orbital angular momentum," *Nat. Commun.* **9**, 4598 (2018).
- T. Ozawa, H. M. Price, A. Amo, N. Goldman, M. Hafezi, L. Lu, M. C. Rechtsman, D. Schuster, J. Simon, O. Zilberberg, and I. Carusotto, "Topological photonics," *Rev. Mod. Phys.* **91**, 015006 (2019).
- Y. Yang, Y.-F. Xu, T. Xu, H.-X. Wang, J.-H. Jiang, X. Hu, and Z.-H. Hang, "Visualization of a unidirectional electromagnetic waveguide using topological photonic crystals made of dielectric materials," *Phys. Rev. Lett.* **120**, 217401 (2018).
- L. He, W. X. Zhang, and X. D. Zhang, "Topological all-optical logic gates based on two-dimensional photonic crystals," *Opt. Express* **27**, 25841–25859 (2019).
- H. Xiong, Q. Wu, Y. Lu, R. Wang, Q. Zhang, J. Qi, J. Yao, and J. Xu, "Polarization-resolved edge states in terahertz topological photonic crystal," *Opt. Express* **27**, 22819–22826 (2019).
- M. J. Mehrabad, A. P. Foster, R. Dost, E. Clarke, P. K. Patil, I. Farrer, J. Heffernan, M. S. Skolnick, and L. R. Wilson, "A semiconductor topological photonic ring resonator," *Appl. Phys. Lett.* **116**, 061102 (2020).
- W. Liu, M. Hwang, Z. Ji, Y. Wang, G. Modi, and R. Agarwal, "2D photonic topological insulators in the visible wavelength range for robust nanoscale photonics," *Nano Lett.* **20**, 1329–1335 (2020).
- H. Kagami, T. Amemiya, S. Okada, N. Nishiyama, and X. Hu, "Topological converter for high-efficiency coupling between Si wire waveguide and topological waveguide," *Opt. Express* **28**, 33619–33631 (2020).
- J. Webber, Y. Yamagami, G. Ducournau, P. Szriftgiser, K. Iyoda, M. Fujita, T. Nagatsuma, and R. Singh, "Terahertz band communications with topological valley photonic crystal waveguide," *J. Lightwave Technol.* **39**, 7609–7620 (2021).
- H. Kagami, T. Amemiya, S. Okada, N. Nishiyama, and X. Hu, "Highly efficient vertical coupling to a topological waveguide with defect structure," *Opt. Express* **29**, 32755–32763 (2021).
- H. Kagami, T. Amemiya, S. Okada, Y. Wang, N. Nishiyama, and X. Hu, "Selective excitation of optical vortex modes with specific charge numbers in band-tuned topological waveguides," *Opt. Lett.* **47**, 2190–2193 (2022).
- G. Siroki, P. A. Huidobro, and V. Giannini, "Topological photonics: from crystals to particles," *Phys. Rev. B* **96**, 041408 (2017).
- S. Barik, A. Karasahin, C. Flower, T. Cai, H. Miyake, W. DeGottardi, M. Hafezi, and E. Waks, "A topological quantum optics interface," *Science* **359**, 666–668 (2018).
- X.-T. He, E.-T. Liang, J.-J. Yuan, H.-Y. Qiu, X.-D. Chen, F.-L. Zhao, and J.-W. Dong, "A silicon-on-insulator slab for topological valley transport," *Nat. Commun.* **10**, 872 (2019).
- M. I. Shalaev, W. Walasik, and N. M. Litchinitser, "Optically tunable topological photonic crystal," *Optica* **6**, 839–844 (2019).
- N. Parappurath, F. Alpegiani, L. Kuipers, and E. Verhagen, "Direct observation of topological edge states in silicon photonic crystals: spin, dispersion, and chiral routing," *Sci. Adv.* **6**, 6–13 (2020).
- D. D. Solnyshkov, A. V. Nalitov, and G. Malpuech, "Kibble-Zurek mechanism in topologically nontrivial zigzag chains of polariton micropillars," *Phys. Rev. Lett.* **116**, 046402 (2016).
- P. St-Jean, V. Goblot, E. Galopin, A. Lemaître, T. Ozawa, L. Le Gratiet, I. Sagnes, J. Bloch, and A. Amo, "Lasing in topological edge states of a one-dimensional lattice," *Nat. Photonics* **11**, 651–656 (2017).
- Z. K. Shao, H. Z. Chen, S. Wang, X. R. Mao, Z. Q. Yang, S. L. Wang, X. X. Wang, X. Hu, and R. M. Ma, "A high-performance topological bulk laser based on band-inversion-induced reflection," *Nat. Nanotechnol.* **15**, 67–72 (2020).
- Z. Q. Yang, Z. K. Shao, H. Z. Chen, X. R. Mao, and R. M. Ma, "Spin-momentum-locked edge mode for topological vortex lasing," *Phys. Rev. Lett.* **125**, 013903 (2020).
- Y. Zeng, U. Chattopadhyay, B. Zhu, B. Qiang, J. Li, Y. Jin, L. Li, A. G. Davies, E. H. Linfield, B. Zhang, and Y. Chong, "Electrically pumped topological laser with valley edge modes," *Nature* **578**, 246–250 (2020).

30. W. Noh, H. Nasari, H.-M. Kim, Q. Le-Van, Z. Jia, C.-H. Huang, and B. Kanté, "Experimental demonstration of single-mode topological valley-Hall lasing at telecommunication wavelength controlled by the degree of asymmetry," *Opt. Lett.* **45**, 4108–4111 (2020).
31. G. Arregui, J. Gomis-Bresco, C. M. Sotomayor-Torres, and P. D. Garcia, "Quantifying the robustness of topological slow light," *Phys. Rev. Lett.* **126**, 027403 (2021).
32. H. R. Kim, M. S. Hwang, D. Smirnova, K. Y. Jeong, Y. Kivshar, and H. G. Park, "Multipolar lasing modes from topological corner states," *Nat. Commun.* **11**, 5758 (2020).
33. H. Zhong, Y. V. Kartashov, A. Szameit, Y. Li, C. Liu, and Y. Zhang, "Theory of topological corner state laser in Kagome waveguide arrays," *APL Photon.* **6**, 040802 (2021).
34. M. Eissa, T. Mitarai, T. Amemiya, Y. Miyamoto, and N. Nishiyama, "Fabrication of Si photonics waveguides by electron beam lithography using improved proximity effect correction," *Jpn. J. Appl. Phys.* **59**, 126502 (2020).
35. T. Amemiya, S. Okada, H. Kagami, N. Nishiyama, Y. Yao, K. Sakoda, and X. Hu, "High-speed infrared photonic band microscope using hyperspectral Fourier image spectroscopy," *Opt. Lett.* **47**, 2430–2433 (2022).
36. S. Peng, N. J. Schilder, X. Ni, J. van de Groep, M. L. Brongersma, A. Alù, A. B. Khanikaev, H. A. Atwater, and A. Polman, "Probing the band structure of topological silicon photonic lattices in the visible spectrum," *Phys. Rev. Lett.* **122**, 117401 (2019).